Behavior of mesoporous silica under 2 MeV electron beam irradiation

Jun Lin, Guillaume Toquer, Clara Grygiel, Sandrine Dourdain, Yannick Guari, Cyrielle Rey, Jérémy Causse, Xavier Deschanels

Behavior of mesoporous silica under 2 MeV electron beam irradiation

Jun LIN,[a] Guillaume TOQUER,[a] Clara GRYGIEL,[b] Sandrine DOURDAIN,[a] Yannick GUARI,[c] Cyrielle REY,[a] Jérémy CAUSSE,[a] Xavier DESCHANELS[a]

[a]*ICSM, CEA, CNRS, ENSCM, Univ Montpellier, Marcoule, France*

[b]*CIMAP, CEA-CNRS-ENSICAEN-UNICAEN Bd. Henri Becquerel, Caen, France*

[c]*ICGM, Univ Montpellier, CNRS, ENSCM, Montpellier, France*

Abstract

This work deals with the evolution of the mesoporous structure of two silicas MCM-41 and SBA-15 under a 2 MeV electron beam as a function of the dose (0 – 5 GGy). For a dose of 2 GGy, the pore volume of the two materials decreases significantly by 40-45%. The irradiation-induced porosity closure is significantly more effective on smaller pores, resulting in a loss of the mesoporous network concerning MCM-41 (pore diameter ~ 3.8 nm) and the conservation of the SBA-15 one (pore diameter ~ 7.0 nm). The mechanism of silica porosity closure/collapse has not been fully identified, but it might result from damage effects as "Knock-on" processes. From a technological point of view, this phenomenon could be exploited for RadioNuclides (RN) encapsulation in a self-evolving porous material.

Keywords: mesoporous silica, ordered material, electron irradiation, radiation damage

1. Introduction

Since its discovery, ordered mesoporous silica materials have attracted considerable attention because of a myriad of potential industrial applications, such as catalysis[1], sensing[2], drug delivery[3], optics[4], ... and nuclear waste management [5-7]. Concerning the last application, researchers have focused intensively on alternate methods employing porous silicates for treating radioactive effluents, including actinides and fission products. Simmons is the first to consider using the porosity of silica glasses for the fixation of radioactive waste[6]. U.S. DOE (Department of Energy) researchers have considered a heat treatment method of transforming crystalline silicotitanate (CST) -type materials for the separation of Cs and/or Sr from radioactive effluents into a waste form matrix [8-10] . Other researchers have been developed the idea of transforming a porous material used for the selective separation of radionuclides into a conditioning matrix, such as microporous tungstate materials[11-14] or mesoporous zirconium titanate[15-19].

Currently, a new method of separation/conditioning of radionuclides (RN) is studied within the ANR Automact project framework [20]. This project aims to show that the separation and the conditioning or the pre-conditioning of RN can be carried out on a solid mesoporous support. Therefore, mesoporous silica is of great interest because it develops high specific surfaces (up to 1000 m^2 / g), which can easily be grafted by organic ligands inside the pores to obtain specific sorption properties of actinides and fission products. Previous work has shown all the potentialities of functionalized mesoporous silicas for the selective separation of radionuclides[21]. The mesoporosity of silicas can be closed under relatively mild conditions by low-temperature heat treatment, mechanical stress application, or even by radiation damage [22-25]. The primary objective of the Automact project is to

assess whether the radiation damage produced by the disintegration of the radionuclides absorbed into the mesoporosity can induce a collapse of the latter, as was observed during external irradiations by ions. This objective will be achieved by studying the effects of the ballistic damage caused by the recoil nucleus associated with the alpha decay of plutonium 238. It is also envisaged studying the effect of the disintegration associated with fission products, i.e., electronic damage. This study focuses on this point by studying the effects of 2 MeV electrons on the evolution of the mesostructure of virgin silica.

Several studies have shown a radiation tolerance of nanoporous metallic materials under certain circumstances[26]. However, the vast majority of works notably related to oxide-based materials [27] have highlighted the collapse of the mesoporous network induced by ion irradiations. Electron beam-induced irreversible atomic displacement in scanning or transmission electron microscopes has also been widely reported [28, 29]. Blanford demonstrated that the relative stability of different varieties of MCM-41 silica under electron beam (at an acceleration voltage of 100 to 300 kV) depends on the synthesis conditions and particularly on the presence of residual surfactants in their structure [28]. No work has, however, explicitly examined the structural evolution (e.g., pore size distribution, wall thickness) of ordered mesoporous silicas in regard to the dose, especially at irradiation conditions representative of the energy corresponding to fission products decays (< 2 MeV).

To evaluate the dimensional change of ordered mesoporous silica in the electronic regime, which is representative of the damage done by beta, gamma disintegrations of fission products, we irradiated pellets obtained by compaction of SBA-15 and MCM-41 powders at low stopping power (~ 1 $MeV.cm^2.g^{-1}$) with a 2 MeV electron beam. The

evolution of the mesoporous structure under irradiation has been addressed to investigate the factors influencing such evolution.

2. Material and methods

2.1. Sample preparation

Two types of ordered mesoporous silica (SBA-15 and MCM-41) were synthesized using the routine self-assembly process of sol-gel chemistry. Pluronic P123 triblock copolymer (Poly (ethylene glycol)-block, Poly (propylene glycol)-block, Poly(ethylene glycol)) and CTAB (cetyltrimethylammonium bromide) were respectively used as structure-directing agents. Tetraethyl orthosilicate (TEOS) was used as a silica precursor. The detailed synthesis steps are listed below. During irradiation, the samples are vertically placed under the electron beam. For that, they are prepared as pellets obtained from the compaction of powders.

2.1.1. Synthesis of SBA-15

The SBA-15 silica was prepared by adapting the procedure used by Zhao *et al.* [30]. 10 g of Pluronic P123 triblock copolymer was dissolved in 262 ml of deionized water, and 50 ml of 37% HCl solution was added to the solution. The mixture was left under continuous stirring for 2 h. Then 22.5 ml of TEOS was added drop by drop with stirring at 40 °C during 1 h. The mixture was kept at 40 °C for about 20 h under static conditions, then heated to 100 °C for 48 h. The solid products were filtered off and washed with deionized water and ethanol repeatedly. The resultant powder was then dried at 100 °C for 5 h, then the temperature was gradually raised to 550 °C over a period of 5 h, and finally, the powder was calcined at 550 °C for another 5 h.

2.1.2. Synthesis of MCM-41

The MCM-41 silica was obtained by a sol-gel process in applying the protocol reported by Kumar et al. [31]. 2.4 g of CTAB was dissolved in 120 ml of deionized water at 30 ℃ and 8 ml of 30% $NH_3 \cdot H_2O$ solution was added to the solution. The mixture was left under continuous stirring for several minutes, then 10 ml of TEOS was added drop by drop during 20 min at room temperature. Then the system was maintained at room temperature for 20 h without stirring. The precipitation was filtered off and washed with water and ethanol

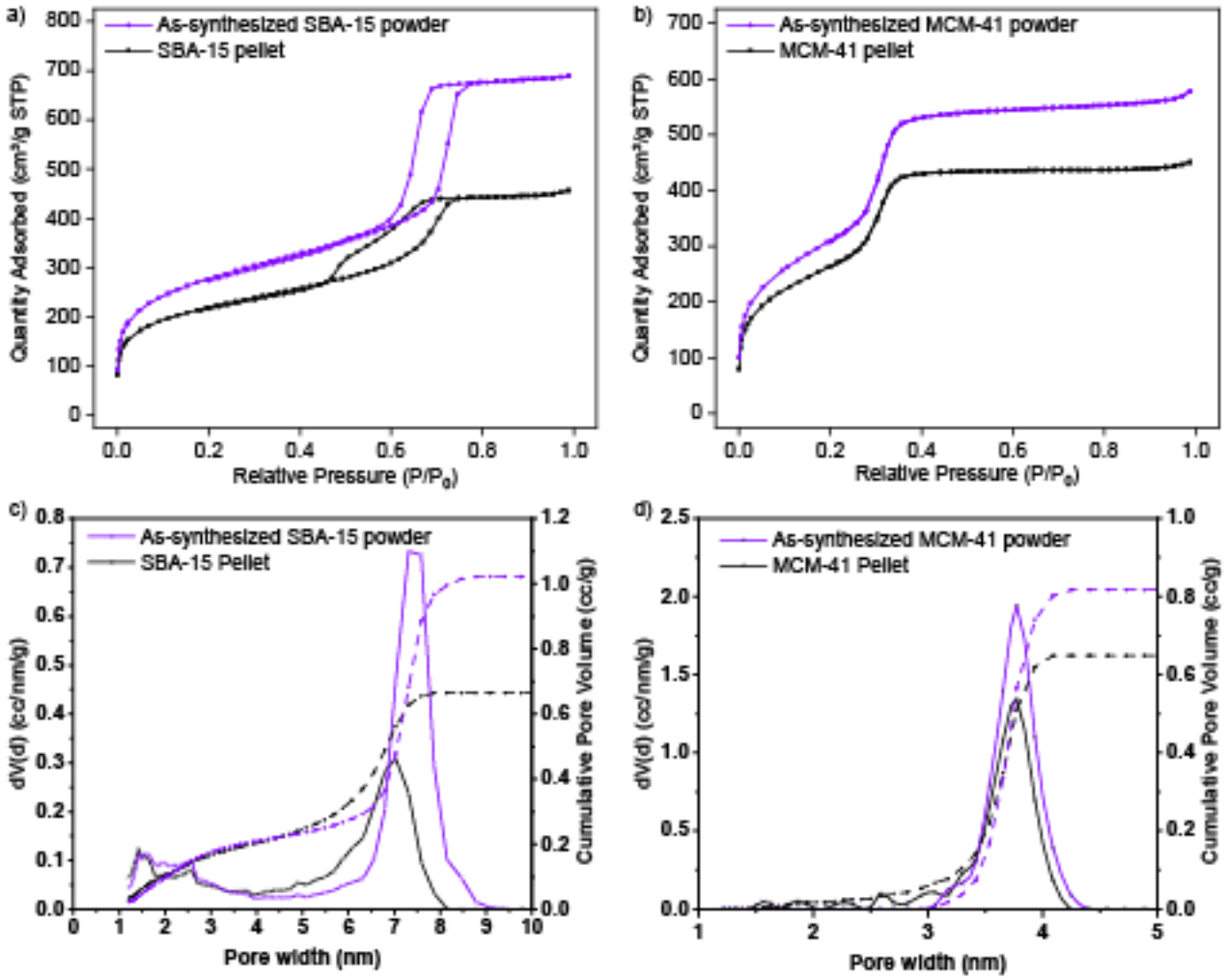

Fig. 1 (a)-(b). Comparison of nitrogen adsorption / desorption isotherms at 77K between powder materials and pellets. (c)-(d) Comparison of pore size distribution between powder materials and pellets.

repeatedly. The resultant powder was dried at 80 ℃ for 1 h and gradually heated to 550 ℃ over 3 h and calcined for another 3 h.

2.1.3. Pellets

The as-synthesized SBA-15 and MCM-41 powders were compacted into pellets (thickness ~ 1 mm, diameter ~ 8 mm) under a pressure of 250 MPa. Then, the pellets were annealed at 400 ℃ for 4 h. Following these treatments, the retention of 2D-hexagonal symmetry of the porous structure within the compacted silica pellets is proven by N_2 sorption isotherms at 77 K (**Fig. 1**), Small-angle X-ray scattering (SAXS) patterns and transmission electron microscopy (TEM) images. The hysteresis loop showed some slight deformation of the cylindrical mesopores of SBA-15 powder and collapse of a minor fraction of the mesopores of MCM-41 powder. Therefore, our subsequent irradiation experiment results will be compared with pristine pellets as a reference. As a result, the alteration of pores caused by the pelleting process will not affect the conclusion of this

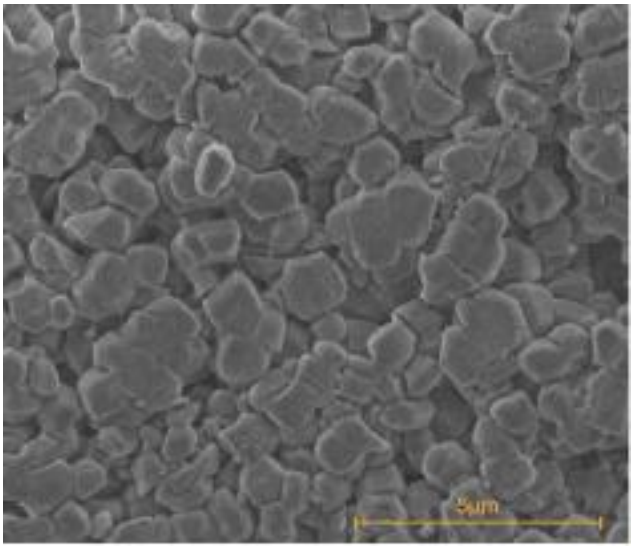

Fig. 2 An SEM image showing the extra-granular pores (macro-pores), caused by the pelleting procedure.

study. Nevertheless, the scanning electron microscopy (SEM) images (**Fig. 2**) of samples have shown the presence of extra-granular pores (macro-pores) due to the pelleting procedure. From the helium pycnometry analysis we can distinguish the volume of these large pores from the small pores (micro and meso-pores) inherently present in the silica powders. More details on this point will be discussed further.

2.2. Electron beam irradiation

The apparatus used for irradiation was a NEC Pelletron at the SIRIUS irradiation facility (Laboratoire des Solides Irradiés, Ecole Polytechnique, France). The energy of electron beam was calculated and adjusted to achieve the energy of 2 MeV at the sample surface after attenuation by the necessary fixing devices. Doses of 0.1, 0.5, 1 and 2 GGy were applied on SBA-15 samples, and irradiations were performed at a flux of 8.5 µA/cm^2,

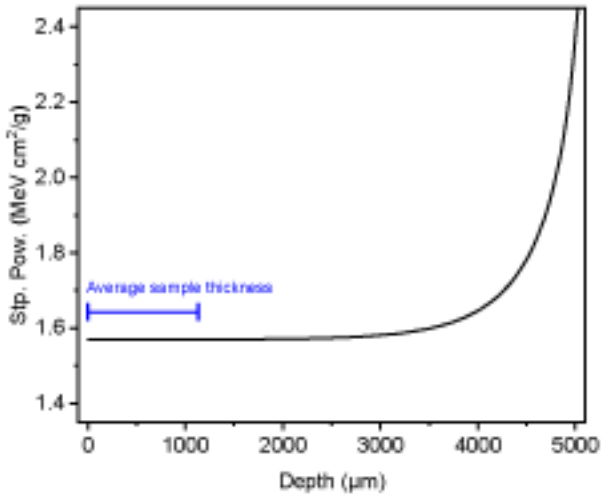

Fig. 3 Stopping power of electrons in mesoporous silicas of density of 2.2 g.cm^{-3}.

which is equivalent to 5.28×10^{13} electrons·cm^{-2}·s^{-1} at room temperature (< 45 °C). MCM-41 were irradiated at 0.1, 0.5, 1, 2 and 5 GGy, with the same experimental conditions.

Under these experimental conditions, ESTAR calculations [32] of the stopping power in the specimen thickness (**Fig. 3**) show that electrons dose deposition can be considered homogeneous for the entire pellet.

2.3. Sample characterizations

2.3.1. Nitrogen adsorption/desorption isotherms

The irradiated samples were characterized by nitrogen gas adsorption/desorption isotherm to obtain specific surface area, micro- and meso-pore size distribution and pore volume. The pellets with known mass were first degassed at 80 ℃ under vacuum for 48 h. The isotherm data were collected at liquid nitrogen temperature (77 K) on Micromeritics Tristar equipment. Structural and textural properties were obtained using the adsorption branch of the isotherm through the non-local density functional theory (NLDFT) method[33-36].

2.3.2. Small-angle X-ray scattering (SAXS)

Small-angle X-ray scattering (SAXS) experiments were conducted using a Guinier-Mering set-up with a 2D image plate detector. The X-ray source was a molybdenum anode, delivering a high-energy monochromatic beam (λ = 0.71 Å, E = 17.4 keV) and providing structural information over scattering vectors q ranging from 0.02 to 3 $Å^{-1}$. The region between the sample and the image plate was purged with flowing helium to avoid air absorption. The data acquisition time was 1800 s, and silver behenate powder in a sealed Kapton piece was used as the scattering vector calibration standard. The experimental resolution was $\Delta q/q$= 0.05. The image azimuthal average was determined using FIT2D

software from ESRF (France), and data corrections (subtractions of empty cell and detector noise) and radial averaging were performed *via* standard procedures.

2.3.3. Density and porosity measurements

The skeletal density of porous silica samples was calculated based on helium pycnometry measurements using a Micromeritics AccuPyc II 1345 helium pycnometer. Before measurement, pellets were degassed at 60 °C for 12 h, and then the density was measured as the average of 10 runs. The skeletal density was calculated according to

$$\rho_{skeletal} = \frac{m_{pellet}}{V_{pycno}} \#(1)$$

The pellets were considered cylindrical, and the apparent volume ($V_{apparent}$) of pellets was measured by vernier caliper. Based on the comparison of the skeletal density and the theoretical density of amorphous silica (~2.3 g.cm^{-3}), the closed porosity of the sample was considered negligible. Consequently, in the subsequent discussion, the total open porosity will be considered as the total porosity. It was calculated according to :

$$\varepsilon_{total} = 1 - \frac{\frac{m_{pellet}}{V_{apparent}}}{\rho_{skeletal}} \#(2)$$

By combining the micropore and mesopore volumes obtained from N_2 isotherm, the respective micropore porosity and mesopore porosity are calculated according to

$$\varepsilon_{micro} = \frac{V_{micro}}{V_{apparent}} \#(3)$$

$$\varepsilon_{meso} = \frac{V_{meso}}{V_{apparent}} \#(4)$$

And finally, the macro-pores (extra-granular pores) porosity are calculated according to

$$\varepsilon_{macro} = \varepsilon_{total} - \varepsilon_{micro} - \varepsilon_{meso} \#(5)$$

The last parameter obtained is the shrinkage (d) of the sample during the irradiation, which is defined as follow:

$$d = \frac{V_{apparent} - V'_{apparent}}{V_{apparent}} \#(6)$$

With $V'_{apparent}$ the apparent volume of the sample after irradiation.

2.3.4. Transmission electron microscopy (TEM)

TEM images were recorded to get some local information on the structural changes induced by electron irradiation. Samples for TEM measurements were deposited from solutions on copper grids. TEM observations were carried out at 100 kV with a JEOL 1200 EXII.

2.3.5. Nuclear magnetic resonance spectroscopy (NMR)

Characterization of the framework of silica gels by nuclear magnetic resonance spectroscopy was already reported by Engelhardt *et al.*[37]. In our work, NMR experiments were performed on a BRUKER ADVANCE 400MHz spectrometer equipped with a CP-MAS VTN4 4mm probe. The Larmor frequencies for ^{1}H and ^{29}Si are 400.1 and 79.5 MHz respectively. The procedure to treat $^{1}H \rightarrow ^{29}Si$ CP and $^{29}Si\ hpdec$ NMR measurements is described as follows: each spectrum was normalized by the integrated intensity and then was deconvoluted to three resonances at ca. -91, -101, -110 ppm, which can be assigned to Q^2, Q^3, Q^4 sites, respectively (See **Section.A** in Supplementary Material).

2.3.6. ATR-FTIR measurement

ATR-FTIR spectroscopy was performed in Perkin Elmer Spectrum 100 Fourier Transform Infrared system containing a 45-degree attenuated total mono reflection (ATR)

device using a KRS-5 crystal. Spectra (6 acquisitions per sample) were acquired between 4000 and 300 cm^{-1} with 4 cm^{-1} resolution. The IR spectra between 1400 and 750 cm^{-1} were deconvoluted as shown in Supplementary Material (**Section.B**).

3. Results and discussions

3.1. Evolution of the porous characteristics of the samples versus irradiation

3.1.1. Helium pycnometry and apparent density of the pellets

The porous characteristics of the samples are shown in **Table 1**. The average skeletal density of the samples is equal to 2.3 ± 0.1 $g.cm^{-3}$. This value is consistent with the theoretical density of amorphous silica (*i.e.*, 2.3 $g.cm^{-3}$). As stated previously, the porosity closure of the samples is very low. The shrinkage of the pellets increases with the radiation dose. This effect is more significant for SBA-15 samples than MCM-41. Unfortunately, the apparent density of the sample MCM-41 irradiated at 5 GGy could not be measured because the sample was broken after irradiation.

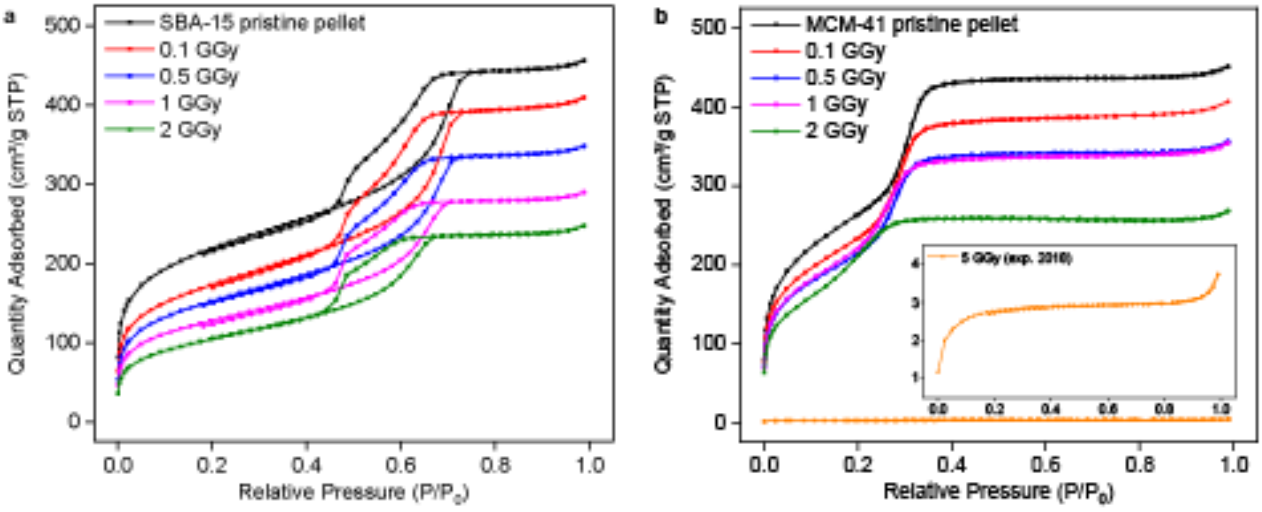

Fig. 4 Nitrogen adsorption / desorption isotherms at 77K of silica pellets, SBA-15 (a) and MCM-41 (b) under 2 MeV electron irradiation.

3.1.2. Nitrogen adsorption/desorption isotherms

The shape of MCM-41 and SBA-15 adsorption isotherms (**Fig. 4**) are characteristic of a type IV curve, indicating the presence of micro- and meso-pores. Comparably, a decrease

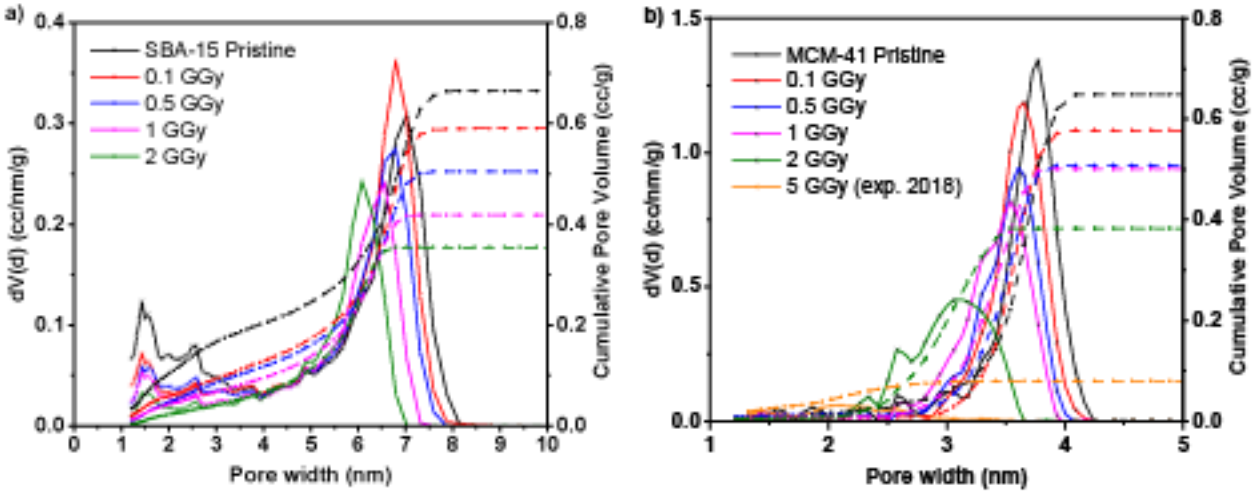

Fig. 5 Pore size distribution of silica samples (a) SBA-15, (b) MCM-41. (Solid line = pore volume, Dash line = cumulative pore volume)

in the adsorbed volumes at saturation is observed as a function of the irradiation dose for the two mesoporous silicas. A change in the shape of the isotherm is observed for 5 GGy (type I isotherm), which indicates a total disappearance of the mesoporosity for this sample.

Fig. 5 shows the pore size distribution calculated from the nitrogen adsorption isotherm

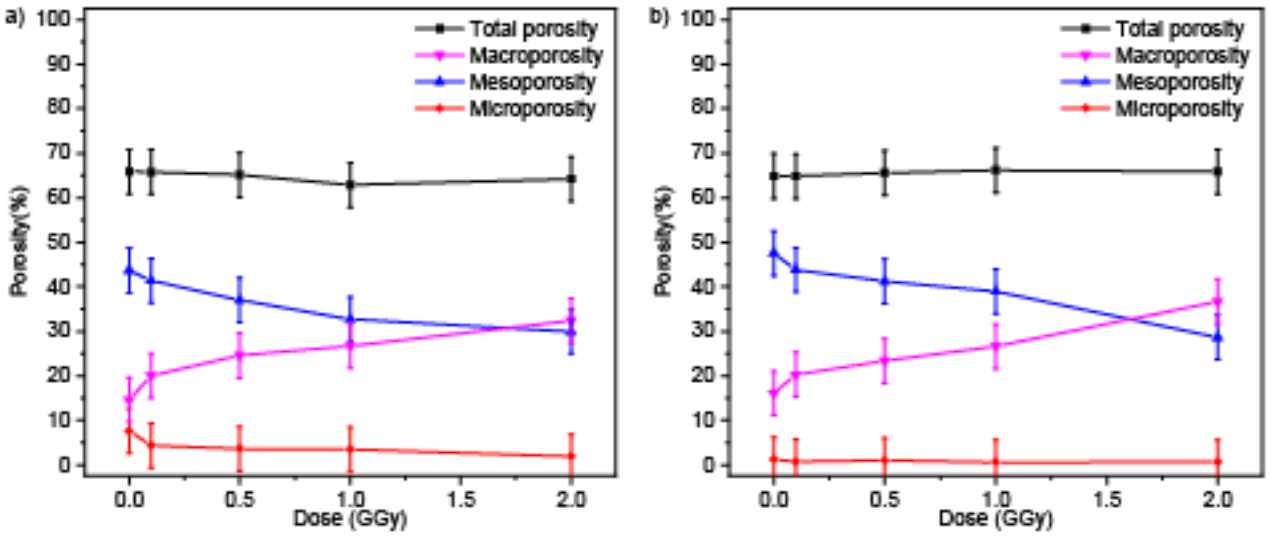

Fig. 6 Evolution of the porosities of the samples with the radiation dose, (a) SBA-15, (b) MCM-41

with the density functional theory (DFT) method. This distribution allows calculating the

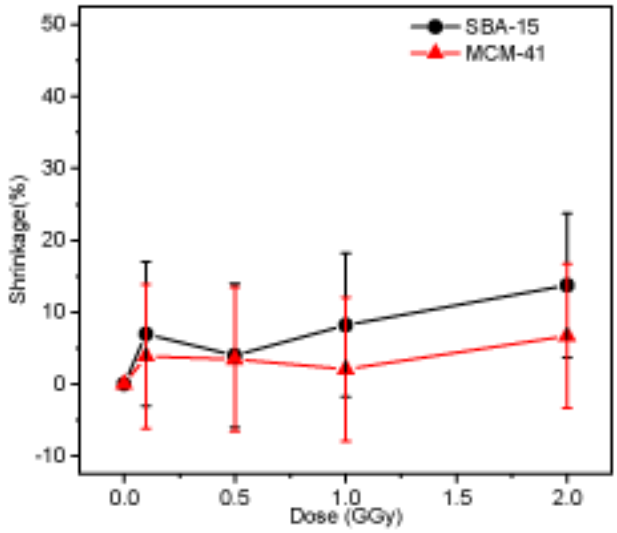

Fig. 7 Evolution of the shrinkage of the samples versus radiation dose

different volumes (V_{micro}, V_{meso}) precisely and, finally, the contribution of each class of porosity (micro, meso, macro) from equations (1-6). These parameters are presented in **Fig. 6** and **Fig. 7** and detailed in the discussion section that follows.

3.1.3. Small-angle X-ray scattering (SAXS)

SAXS measurements performed on pellets after electron beam irradiation are shown in **Fig. 8**. The scattered intensity displays three well-resolved peaks indexed as (100), (110),

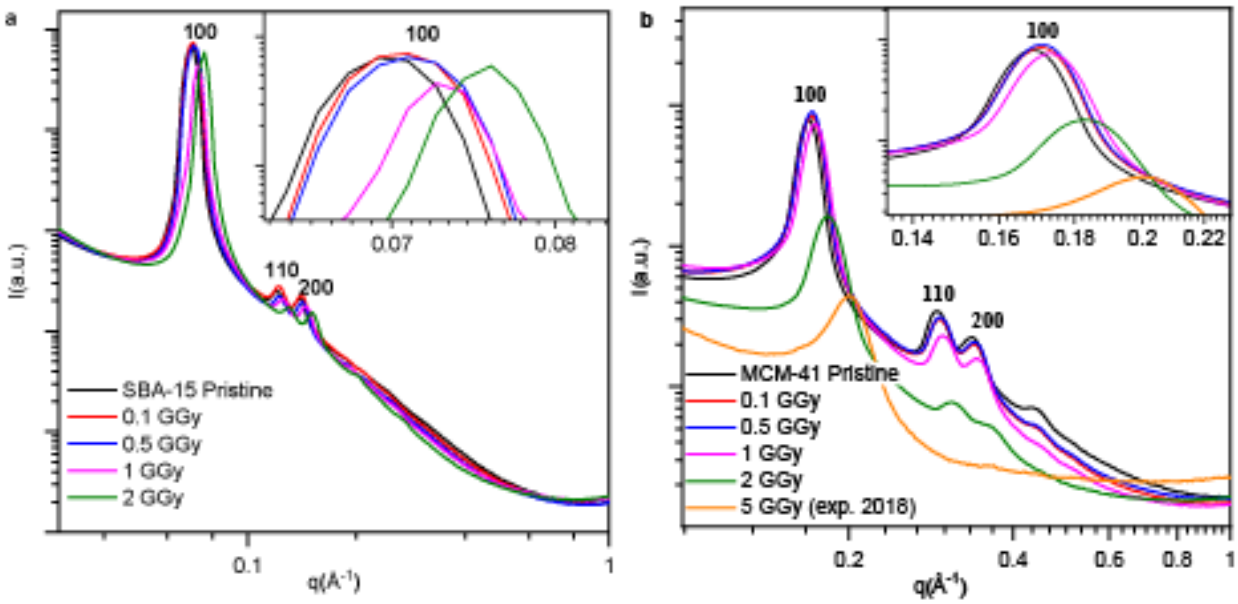

Fig. 8 Small angle X-ray scattering spectra of silica pellets, SBA-15 (a) and MCM-41 (b) under 2 MeV electron irradiation.

(200), which can be associated with p6mm hexagonal symmetry. Remarkably, no significant change was observed in SBA-15 structure up to 2 GGy, while MCM-41, a decrease in the intensities of the peaks occurs at 2 GGy with a complete extinction at 5 GGy. For both samples, the structural peaks are shifted to high q values under irradiation, which indicates a decrease of the lattice parameter a_0. Being equal to the average distance between the pores (for 2D hexagonal structure $a_0 = 2d_{100}/\sqrt{3}$, where $d_{100} = 2\pi/q_{100}$),

this decrease of a_0 may result from a decrease of the silica wall or of the pore diameter, or both. Through correlating the various characterization data, this impact will be clearly understood in the following.

3.2. Structural characterization of silica

3.2.1. Nuclear magnetic resonance spectroscopy

Nuclear magnetic resonance spectroscopy was used to evaluate the modification of the silica network. The results obtained from the ^1H and $^1H \rightarrow ^{29} Si$ CP analysis are summarized (see **Section.C** in Supplementary Material). However, these results are not representative of the bulk volume for the following reasons: Firstly, CP-MAS is quite dependent on the hydration state of the sample, which is independent of irradiation, which means that the spectra are more challenging to compare. Secondly, surface protons can induce faster relaxation of nearby silicon atoms. Therefore, we favored high-power decoupling with magic angle spinning (HPDEC – MAS) NMR direct ^{29}Si acquisition. As shown in **Fig. 9**, the Q^n group analysis was employed with direct ^{29}Si MAS NMR acquisition. No significant change was observed in the chemical shift of Q^n peaks. It must be noted that the chemical shifts observed are different from those known for α-quartz[38]. This could give a hint that there is no radiation-induced crystallization. A slight increase of the Q^3/Q^4 ratio is observed when going from the as-synthesized material to the irradiated one. The most likely reason for this increase is the breaking of some $Si-(OSi)_4$ structural units into the $Si-(OSi)_3O^-H^+$ structures during the electron beam radiation. However, with a small sample size, caution must be applied, as the variation is ridiculously small

compared to the change observed in porosities. Extensively, SiO_2 networks tend to remain at a steady-state, with no significant accumulation of defects.

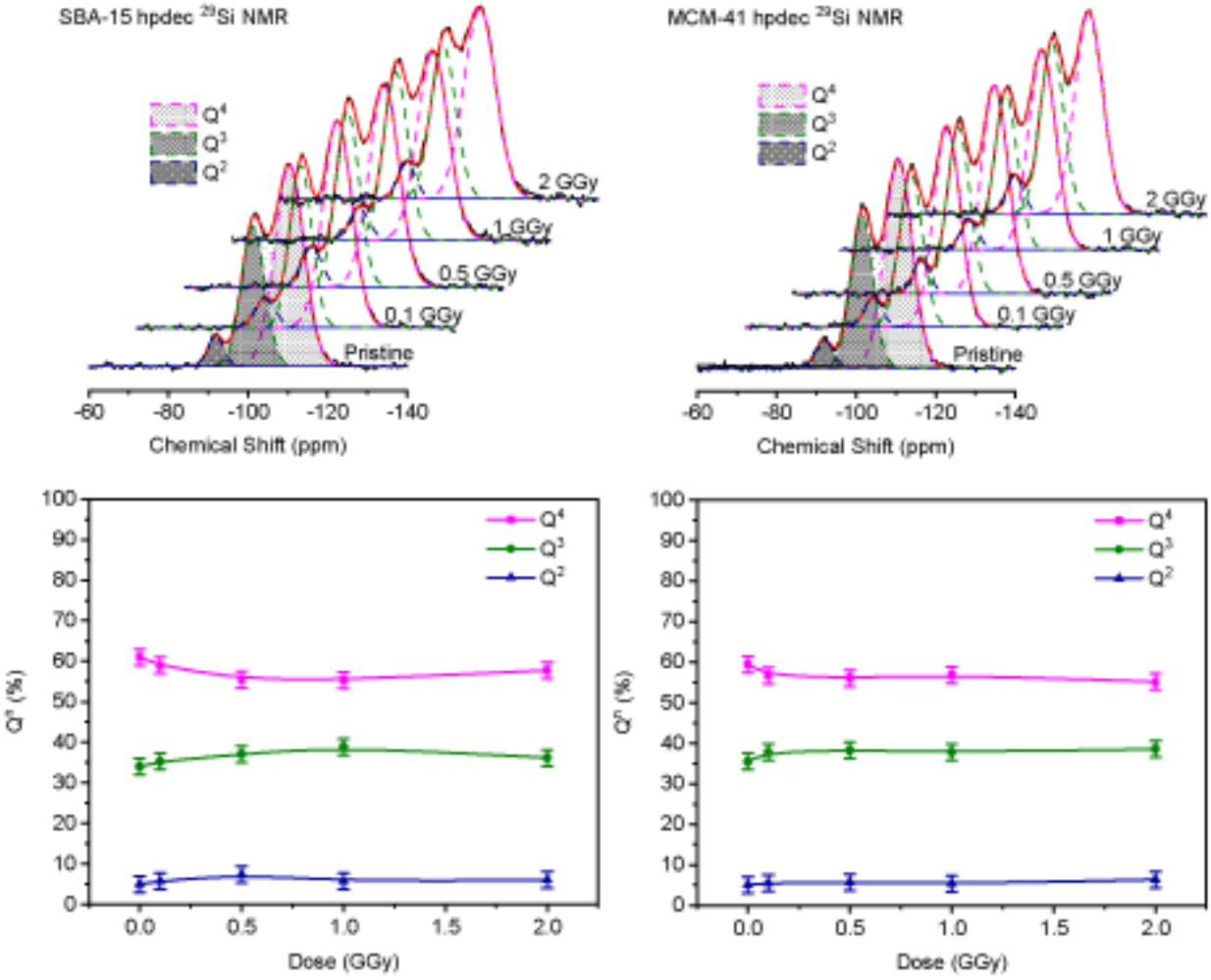

Fig. 9 Deconvolution of HPDEC-MAS ^{29}Si NMR spectrum and evolution of the Q^n sites.

3.2.2. ATR-FTIR measurement

A zoom on the 750-1400 cm^{-1} region of the deconvoluted ATR-FTIR spectrum shows the Si-OH, and SiO_2 vibration modes. However, LO_4, TO_4 and TO_3 mode vibrations might not represent their real population as the decomposition of the "shoulder region" has been controversial and inconclusive in previous studies. For the discussion afterward, only the

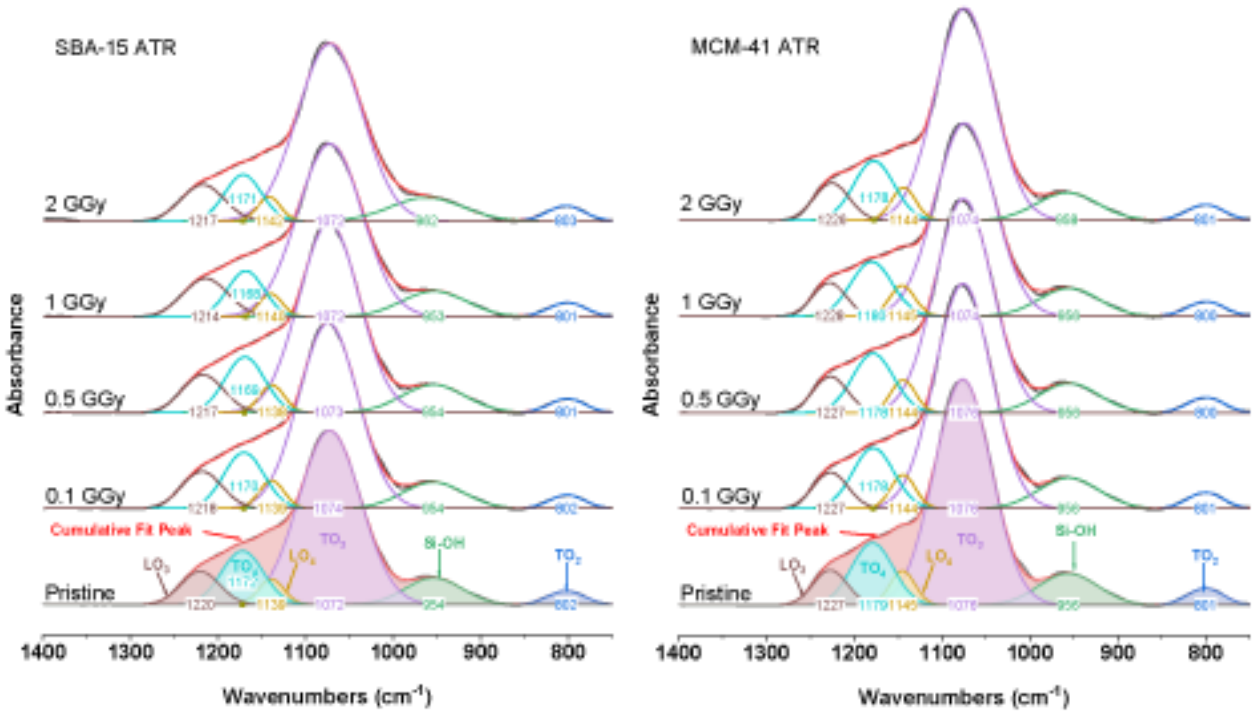

Fig. 10 Deconvoluted ATR-FTIR spectra between 1400 and 750 cm^{-1} and reconstituted spectra after curve fitting.

TO_3 vibrations located around 1074 cm^{-1} will be compared after irradiation. Many scholars hold the view that the position of the TO_3 peak is linked to the density of the SiO_2 network, and its shift to lower wavenumber (redshift) is assigned to a reduction in density. As can be seen from **Fig. 10**, the position of the TO_3 peak did not change within the analytical error, implying that the densification of the SiO_2 network is almost absent or negligible, which is in agreement with the results of NMR.

3.3. Transmission electron microscopy (TEM)

Though nitrogen gas sorption related techniques, helium pycnometry, and X-ray scattering reveal averaged structures, TEM imaging is much more accurate for determining

local structures and default accumulations. Under the experimental irradiation conditions, even though the previous results indicated that most of the mesoporous structures were not damaged, TEM images in **Fig. 11**. show significant structural collapse when higher doses are applied.

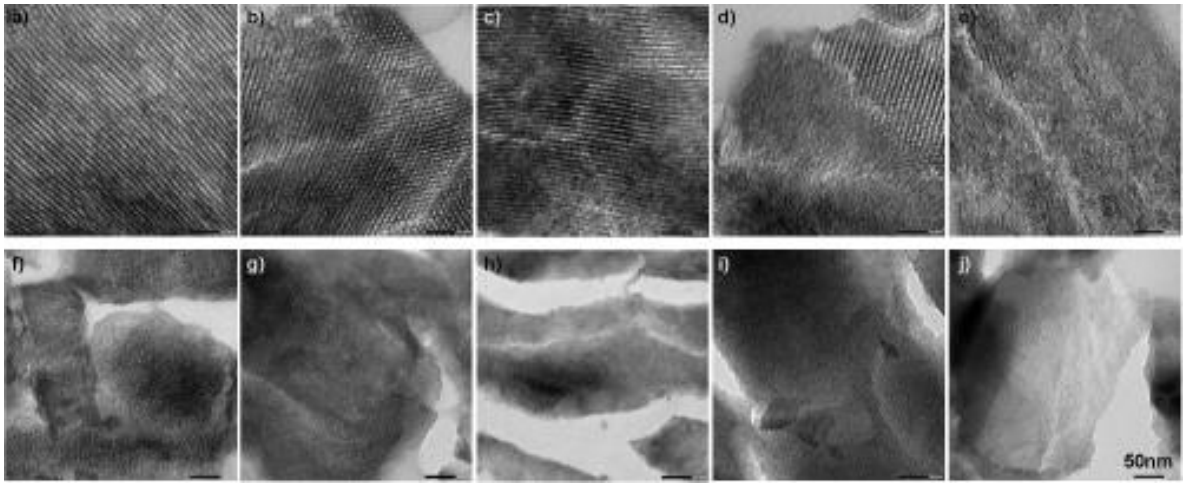

Fig. 11 TEM images of SBA-15 samples: a)-e) sequentially represent pristine - 0.1 - 0.5 – 1.0 – 2.0 GGy and MCM-41 samples: f)-j) sequentially represent pristine - 0.1 - 0.5 – 1.0 – 2.0 GGy.

4. Discussion

4.1. Volume change

The first conclusion is that the innate porosities (micro and mesoporosity) decrease with the increase of the radiation dose. Concomitantly, an increase in the shrinkage of the samples and an increase in the macroporosity volume are observed. It can be assumed that the mesoporous silica grains observed in **Fig. 2** have densified, generating an increase in intergranular porosity, i.e., macroporosity. These volume changes lead to internal stresses within the pellets, inducing few micro-cracks as observed by SEM (**Fig. 12**). However, these observations do not highlight an important density of microcracking. It seems that the

mesoporous silicas obtained by the sol-gel route exhibit some plasticity, allowing relaxing these constraints partially. This increase in macroporosity could be problematic for the intended application as regards the leaching of these materials. However, we must keep in mind that the surface area of macropore is ridiculously small compared to the specific surface area of micro and mesopores, and those marcopores are relatively easy to reseal

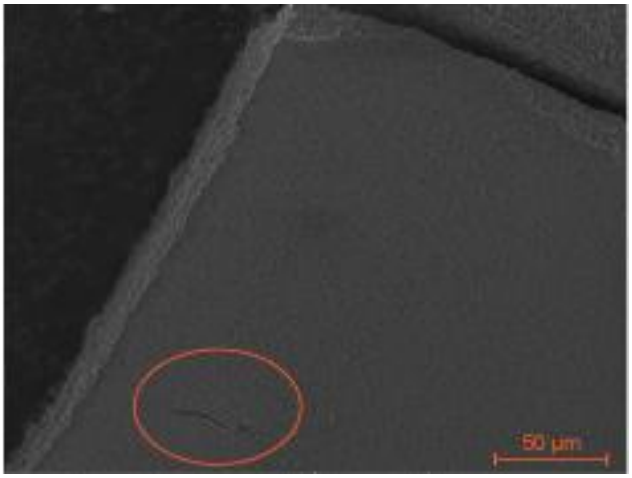

Fig. 12 Micro-cracks observed by SEM in the silica sample.

with the help of other means. These aspects are studied within the framework of ANR Automact and will give rise to a future publication.

The second important result obtained from this analysis is the apparent trend of decreasing mesopore diameter. This change occurs from the lowest doses (0.1 GGy) but does not impact the global structure, even at 2 GGy dose, as shown by the shape of N_2 adsorption isotherm curves (**Fig. 4)**. **Fig. 5** also indicates that SBA-15 keeps a narrow pore-size distribution, though it becomes larger for MCM-41. It suggests that SBA-15 still possesses an ordered structure, while the mesoporous structure of MCM-41 is slightly

disrupted. This result is supported by SAXS measurements (**Fig. 8**) and TEM observations (**Fig. 11**) which shows a loss of the organization of the MCM-41 pore network for the highest dose.

The third result concerns silica ligands. The evolution of the lattice parameter a_0 presents the same trends as the one of the pore size (**Table 1**), which on a first look confirms the dose-dependent collapse of the mesoporous structure. However, the radiation effect on pore size and silica wall thickness can be decorrelated due to the relation of the different characterization results. The apparent wall thickness W can be calculated [26] from the lattice parameter a_0 and the pore radius r determined via SAXS and nitrogen sorption using the equation:

$$W = a_0 - 2r \quad (7)$$

As presented in **Table 1**, the wall thickness W increases with the radiation dose for MCM-41 while does not significantly evolve for SBA-15. This result shows that the collapse of the structure is mainly due to a pore size decrease for both structures, and confirms the more significant structural disruption of the MCM-41 compared to SBA-15.

The structure of the silica walls was further characterized by NMR and FTIR for the two mesoporous silicas. No significant modification was observed with the irradiation dose, which is consistent with the theoretical density value obtained from pycometric density measurements. Bibliographic results indicate that the amorphous silica densification under irradiation saturates to a value close to 3% [39]. This saturation effect depends on the nature of the projectile, *i.e.*, electrons, ions, neutrons, and more precisely on the interactions (ballistic or electronic) [40]. For electronic interaction, the dose necessary for the evolution

of density is greater than 10 GGy and the value of 3% swelling is obtained at approximately 30 GGy. The maximum dose at which the samples were irradiated in this study is much lower, which explains why no significant change was detected.

4.2. Collapse mechanism

In recent years, the potential applications of mesoporous materials in the nuclear field have been booming [5], but only a few works have focused on the evolution of nanoporosity under electronic or ionic irradiation. The idea that mesoporosity might be favorable for recombination of irradiation defects due to proximity to surfaces has not been conclusively demonstrated. A few studies on the irradiation of metallic foams show tolerance of some nanoporous metals to irradiation due to the recombination of the defects. This tolerance was dependent on the size of the pores [26, 41].

Studies carried out on all mesoporous oxides show a collapse of the mesoporous structure under irradiation with ions. These works concern damage of ballistic type [27, 42-44] or under very strong electronic excitations (tracks formation regime) [45-47] which do not correspond to the irradiation conditions described in this study. The only work related to the damage of mesoporous silicas MCM-41 by electrons was proposed by Blanford et al. [28]. However, the irradiation conditions are quite different from those investigated in this study since the samples were irradiated in a TEM, i.e., at a lower energy (100-300 kV) and higher flow rates. Under these conditions, Blanford proposed a predominantly radiolytic damage mechanism, with an important contribution from the heating of the samples by the electron beam. Despite the fact that different irradiation conditions, we attempted to compare with the mechanisms proposed by Blanford.

First, the sample-heating process does not appear to be operative in our case since the samples are cooled during irradiation, ensuring a maximum specimen temperature of 45 °C. In addition, experimental results performed in our laboratory have shown complete densification and loss of organization of the mesoporous network (SAXS measurement) of SBA-15 heated to 1000 °C, while MCM-41 retains both a fraction of pore volume and its pore network under the same conditions. This result is actually the opposite of what was observed when the samples were irradiated with 2 MeV electrons.

Second, we use the model proposed by Marples in the 1980s to estimate a cross-section of the process and compare it with the results of Blanford. This model was first used to explain the swelling of glasses under internal irradiation.[48] and later on external irradiation by other researchers[49, 50]. This assertion was based on the assumption that a critical event (alpha decay for internal radiation or ion passage for external irradiation) induces a saturation of the irradiation damage in the impacted area. In other words, it considers that an area already impacted can no longer be damaged by a second event. It is also assumed that the change in property, swelling or densification, is proportional to the fraction of damaged volume. With this second hypothesis, Marples's equation can be written as:

$$\frac{\Delta\rho}{\rho} = \left(\frac{\Delta\rho}{\rho}\right)_{sat}\left(1 - \exp(-\upsilon R t)\right) \quad (7)$$

$\Delta\rho$ is the evolution of macroscopic properties (pore volume, thickness, density, mechanical property, etc.). The index "sat" means the saturation state. In this work, the term $\upsilon R t$ can be replaced by $\sigma\Phi$ where σ is the cross-section, and Φ is the fluence.

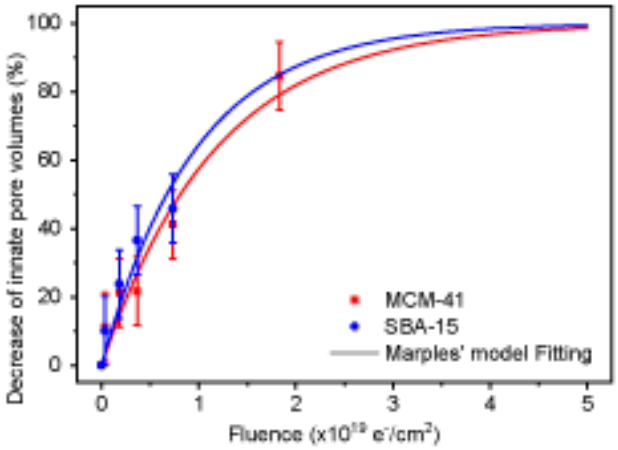

Fig. 13 Pore volumes decrease as a function of fluence for SBA-15 and MCM-41.

In Figure 12, the evolution of the innate porosities (micro and mesoporosity) (PV) of the mesoporous sample with the fluence is fitted using this model considering a non-porous material (100% compacted) as the final state. The damage cross-sections obtained from the fit are $(9 \pm 2) \times 10^{-20} cm^2$ for MCM-41 and $(1.4 \pm 0.6) \times 10^{-19} cm^2$ for SBA-15, respectively.

The present study estimated a damage cross-section in the order of $10^{-20} \sim 10^{-19} cm^2$.This is not in the same order of magnitude of the radiolytic damage cross-section estimated for silica by Blanford *et al.* but rather close to the estimated knock-on damage cross-section. These findings provide a strong empirical confirmation that a change in the dominant damage mechanism from radiolytic to knock-on occurs at electron energy between 100 keV and 2.5 MeV [51], although the structural evolution did not appear different.

Regarding the research methods, some limitations need to be acknowledged. First, our calculation of cross-section is based on several hypotheses mentioned above. Second, since this study was limited to only one electron energy, it could not include an in-depth comparison of radiolytic and knock-on damage mechanisms. A natural progression of this work is to investigate the material behavior under different ratios of collision and radiative stopping powers. Future work would be interesting to repeat the experiments described here using 0.6, 1.2 and 2.4 MeV electrons, with collision and radiative ratios. The ratio is

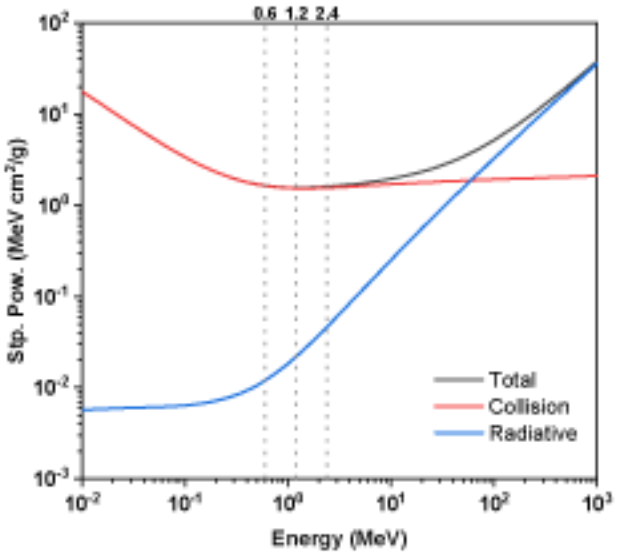

Fig. 14 Stopping power of electrons (collision and radiative) in silicon dioxide.

varying as shown in **Fig. 14**.

5. Conclusions

SBA-15 and MCM-41 mesoporous silicas are both susceptible to radiation damage from 2 MeV electron irradiation. Up to a dose of 5 GGy, this damage affects the porous network (change in volume, collapse) and does not affect the density of the silica walls. This

irradiation has a greater impact on the porous structure, exhibiting a smaller pore size leading to complete amorphization of the MCM-41 sample, while the SBA-15 is less affected. At a macroscopic scale, this phenomenon results in a withdrawal of the pellets and jointly in an increase of their macroporosity leading to the appearance of certain microcracks. The overall nanoporous volume (mesoporous + microporous) of samples SBA-15 and MCM-41 was affected comparably up to a dose of 2 GGy, respectively $\Delta V/V$: ~ 41% against ~ 45%. Differences were observed in terms of meso and microporosity. The microporosity of the SBA-15 pellets almost completely disappeared and a sharp decrease in the volume of mesoporosity was observed, while the hexagonal structure is well preserved. A greater reduction in the mean diameter of the MCM-41 mesopore was observed, leading to a disappearance of their hexagonal structure.

The origin of this collapse is not fully understood, but the ballistic effects appear to be effective in this process. Electron irradiations at different energies from 0.5 to 2 MeV are in progress to assess the influence of the "knock-on" process more precisely.

The potential of such materials to be functionalized for the encapsulation of the RNs and for obtaining a waste conditioning matrix is given by the extremely large specific surface area. Considering those congenital properties, the radiation-induced collapse of those micro and mesoporous structures provides fundamental research support for this concept.

Acknowledgments

This work is partially funded by the French Research Agency within the framework of the AUTOMACT project under Grant Number ANR-18-CE05-0016-02. We acknowledge

the French EMIR&A network for provision of irradiation beam time and we would like to thank Dr. R. Grasset and Dr. A. Alessi for assistance in using the SIRIUS facility. The authors thank S. Maynadié and A. Jonchère for their contributions to the NMR and FTIR measurements. Thanks also to Dr. C.M. Singaravelu and Dr. H. Sour for discussions.

Table 1 Densities, porosities and shrinkage of the samples versus irradiation dose (2 MeV electron beam).

		Before irradiation	After irradiation									
	Dose (GGy)	$\rho_{apparent}$ ($g.cm^{-3}$)	$\rho'_{apparent}$ ($g.cm^{-3}$)	$\rho_{skeleton}$ ($g.cm^{-3}$)	$\varepsilon_{tot.}$ (%)	$\varepsilon_{micro.}$ (%)	$\varepsilon_{meso.}$ (%)	$\varepsilon_{macro.}$ (%)	D (%)	W (nm)	a_0 (nm)	D (nm)
MCM-41	0	0.74		2.12	65	1	48	16	--	0.5	4.3	3.8
	0.1	0.72	0.76	2.15	65	1	44	20	3.9	0.6	4.3	3.7
	0.5	0.72	0.82	2.38	66	1	41	23	3.5	0.6	4.2	3.6
	1.0	0.74	0.77	2.28	66	1	39	27	2.1	0.7	4.2	3.5
	2.0	0.70	0.76	2.23	66	1	29	37	6.7	0.9	4.0	3.1
	5.0	--	--	--	--	--	--	--	--	1.5	3.6	2.1
SBA-15	0	0.76		2.23	66	8	44	15	--	3.4	10.4	7.0
	0.1	0.71	0.76	2.21	66	4	41	20	7.0	3.5	10.3	6.8
	0.5	0.73	0.79	2.27	65	4	37	25	4.0	3.5	10.2	6.7
	1.0	0.77	0.85	2.28	63	3	33	27	8.2	3.5	9.9	6.4
	2.0	0.77	0.88	2.45	64	2	30	32	13.7	3.5	9.6	6.1

References

[1] A. Taguchi, F. Schüth, Ordered mesoporous materials in catalysis, Microporous Mesoporous Mater., 77 (2005) 1-45. http://dx.doi.org/10.1016/j.micromeso.2004.06.030

[2] F. Goettmann, A. Moores, C. Boissiere, P. Le Floch, C. Sanchez, A selective chemical sensor based on the plasmonic response of phosphinine-stabilized gold nanoparticles hosted on periodically organized mesoporous silica thin layers, Small, 1 (2005) 636-639. http://dx.doi.org/10.1002/smll.200500037

[3] J.F. Chen, H.M. Ding, J.X. Wang, L. Shao, Preparation and characterization of porous hollow silica nanoparticles for drug delivery application, Biomaterials, 25 (2004) 723-727. http://dx.doi.org/10.1016/s0142-9612(03)00566-0

[4] P. Yang, G. Wirnsberger, H.C. Huang, S.R. Cordero, M.D. McGehee, B. Scott, T. Deng, G.M. Whitesides, B.F. Chmelka, S.K. Buratto, G.D. Stucky, Mirrorless lasing from mesostructured waveguides patterned by soft lithography, Science, 287 (2000) 465-468. http://dx.doi.org/10.1126/science.287.5452.465

[5] P. Makowski, X. Deschanels, A. Grandjean, D. Meyer, G. Toquer, F. Goettmann, Mesoporous materials in the field of nuclear industry: applications and perspectives, New J. Chem., 36 (2012) 531-541. http://dx.doi.org/10.1039/c1nj20703b

[6] J.H. Simmons, P.B. Macedo, A. Barkatt, T.A. Litovitz, Fixation of radioactive waste in high silica glasses, Nature, 278 (1979) 729-731. http://dx.doi.org/10.1038/278729a0

[7] H.-C. zur Loye, T. Besmann, J. Amoroso, K. Brinkman, A. Grandjean, C.H. Henager, S. Hu, S.T. Misture, S.R. Phillpot, N.B. Shustova, H. Wang, R.J. Koch, G. Morrison, E. Dolgopolova, Hierarchical Materials as Tailored Nuclear Waste Forms: A Perspective, Chem. Mater., 30 (2018) 4475-4488. http://dx.doi.org/10.1021/acs.chemmater.8b00766

[8] M. Nyman, T.M. Nenoff, Y. Su, M.L. Balmer, A. Navrotsky, H. Xu, New Crystalline Silicotitanate (CST) Waste Forms: Hydrothermal Synthesis and Characterization of CS-SI-TI-O Phases, MRS Proceedings, 556 (1999) 71. http://dx.doi.org/10.1557/PROC-556-71

[9] Y. Su, M.L. Balmer, L. Wang, B.C. Bunker, M. Nyman, T. Nenoff, A. Navrotsky, Evaluation of thermally converted silicotitanate waste forms, MRS Proceedings, 556 (1999) 77. http://dx.doi.org/10.1557/PROC-556-77

[10] T. Tomasberger, A.C. Veltkamp, A.S. Booij, U.W. Scherer, Radiocesium removal from high level liquid waste and immobilisation in sodium silicotitanate for geological disposal, Radiochimica Acta, 89 (2001) 145-150. http://dx.doi.org/doi:10.1524/ract.2001.89.3.145

[11] C.S. Griffith, V. Luca, Ion-Exchange Properties of Microporous Tungstates, Chem. Mater., 16 (2004) 4992-4999. http://dx.doi.org/10.1021/cm049335w

[12] V. Luca, C.S. Griffith, E. Drabarek, H. Chronis, Tungsten bronze-based nuclear waste form ceramics. Part 1. Conversion of microporous tungstates to leach resistant ceramics, J. Nucl. Mater., 358 (2006) 139-150. http://dx.doi.org/https://doi.org/10.1016/j.jnucmat.2006.06.017

[13] C.S. Griffith, F. Sebesta, J.V. Hanna, P. Yee, E. Drabarek, M.E. Smith, V. Luca, Tungsten bronze-based nuclear waste form ceramics. Part 2: Conversion of granular microporous tungstate–polyacrylonitrile (PAN) composite adsorbents to leach resistant ceramics, J. Nucl. Mater., 358 (2006) 151-163. http://dx.doi.org/https://doi.org/10.1016/j.jnucmat.2006.06.018

[14] V. Luca, E. Drabarek, H. Chronis, T. McLeod, Tungsten bronze-based nuclear waste form ceramics. Part 3: The system Cs0.3MxW1−xO3 for the immobilization of radio cesium, J. Nucl. Mater., 358 (2006) 164-175. http://dx.doi.org/https://doi.org/10.1016/j.jnucmat.2006.06.019
[15] V. Luca, W.K. Bertram, J. Widjaja, D.R.G. Mitchell, C.S. Griffith, E. Drabarek, Synthesis of mesoporous zirconium titanates using alkycarboxylate surfactants and their transformation to dense ceramics, Microporous Mesoporous Mater., 103 (2007) 123-133. http://dx.doi.org/https://doi.org/10.1016/j.micromeso.2007.01.024
[16] C.S. Griffith, M.D.L. Reyes, N. Scales, J.V. Hanna, V. Luca, Hybrid Inorganic−Organic Adsorbents Part 1: Synthesis and Characterization of Mesoporous Zirconium Titanate Frameworks Containing Coordinating Organic Functionalities, ACS Applied Materials & Interfaces, 2 (2010) 3436-3446. http://dx.doi.org/10.1021/am100891u
[17] C.S. Griffith, G.D. Sizgek, E. Sizgek, N. Scales, P.J. Yee, V. Luca, Mesoporous Zirconium Titanium Oxides. Part 1: Porosity Modulation and Adsorption Properties of Xerogels, Langmuir, 24 (2008) 12312-12322. http://dx.doi.org/10.1021/la801464s
[18] G.D. Sizgek, E. Sizgek, C.S. Griffith, V. Luca, Mesoporous Zirconium Titanium Oxides. Part 2: Synthesis, Porosity, and Adsorption Properties of Beads, Langmuir, 24 (2008) 12323-12330. http://dx.doi.org/10.1021/la801490k
[19] G.D. Sizgek, C.S. Griffith, E. Sizgek, V. Luca, Mesoporous Zirconium Titanium Oxides. Part 3. Synthesis and Adsorption Properties of Unfunctionalized and Phosphonate-Functionalized Hierarchical Polyacrylonitrile-F-127-Templated Beads, Langmuir, 25 (2009) 11874-11882. http://dx.doi.org/10.1021/la9015299
[20] Project-ANR-18-CE05-0016, solid fixation and auto-conditioning of actinide elements coming from contaminated liquid outflows, 2018. http://anr.fr/Project-ANR-18-CE05-0016
[21] G.E. Fryxell, Y. Lin, S. Fiskum, J.C. Birnbaum, H. Wu, K. Kemner, S. Kelly, Actinide Sequestration Using Self-Assembled Monolayers on Mesoporous Supports, Environmental Science & Technology, 39 (2005) 1324-1331. http://dx.doi.org/10.1021/es049201j
[22] A. Alessi, G. Buscarino, S. Agnello, F. Messina, L. Sciortino, M. Cannas, F.M. Gelardi, Effects of Pressure, Thermal Treatment, and O2 Loading in MCM41, MSU-H, and MSU-F Mesoporous Silica Systems Probed by Raman Spectroscopy, J. Phys. Chem. C, 119 (2015) 27434-27441. http://dx.doi.org/10.1021/acs.jpcc.5b10206
[23] A. Hertz, V. FitzGerald, E. Pignotti, J.C. Knowles, T. Sen, I.J. Bruce, Preparation and characterisation of porous silica and silica/titania monoliths for potential use in bone replacement, Microporous Mesoporous Mater., 156 (2012) 51-61. http://dx.doi.org/10.1016/j.micromeso.2012.02.004
[24] T. Tatsumi, K.A. Koyano, Y. Tanaka, S. Nakata, Mechanical stability of mesoporous materials, MCM-48 and MCM-41, J. Porous Mater., 6 (1999) 13-17. http://dx.doi.org/10.1023/a:1009682915127
[25] X. Zhang, X. Yu, B. Zhou, W. Luo, W. Jiang, W. Jiang, Z. Shen, L. Wang, Y. Yuxiang, Sinterability Enhancement by Collapse of Mesoporous Structure of SBA-15 in Fabrication of Highly Transparent Silica Glass, J. Am. Ceram. Soc., 98 (2015) 1056-1059. http://dx.doi.org/10.1111/jace.13529

[26] E.M. Bringa, J.D. Monk, A. Caro, A. Misra, L. Zepeda-Ruiz, M. Duchaineau, F. Abraham, M. Nastasi, S.T. Picraux, Y.Q. Wang, D. Farkas, Are nanoporous materials radiation resistant?, Nano Lett., 12 (2012) 3351-3355. http://dx.doi.org/10.1021/nl201383u
[27] Y. Lou, S. Dourdain, C. Rey, Y. Serruys, D. Simeone, N. Mollard, X. Deschanels, Structure evolution of mesoporous silica under heavy ion irradiations of intermediate energies, Microporous Mesoporous Mater., 251 (2017) 146-154. http://dx.doi.org/10.1016/j.micromeso.2017.05.057
[28] C.F. Blanford, C.B. Carter, Electron radiation damage of MCM-41 and related materials, Microsc. Microanal., 9 (2003) 245-263. http://dx.doi.org/10.1017/S1431927603030447
[29] N. Jiang, Electron beam damage in oxides: a review, Rep. Prog. Phys., 79 (2016) 016501. http://dx.doi.org/10.1088/0034-4885/79/1/016501
[30] D. Zhao, J. Feng, Q. Huo, N. Melosh, G.H. Fredrickson, B.F. Chmelka, G.D. Stucky, Triblock copolymer syntheses of mesoporous silica with periodic 50 to 300 angstrom pores, Science, 279 (1998) 548-552. http://dx.doi.org/10.1126/science.279.5350.548
[31] D. Kumar, K. Schumacher, C. du Fresne von Hohenesche, M. Grün, K.K. Unger, MCM-41, MCM-48 and related mesoporous adsorbents: their synthesis and characterisation, Colloids Surf. A Physicochem. Eng., 187-188 (2001) 109-116. http://dx.doi.org/10.1016/s0927-7757(01)00638-0
[32] NIST Estar, Stopping Power and Range Tables for Electrons.
[33] C. Lastoskie, K.E. Gubbins, N. Quirke, Pore size distribution analysis of microporous carbons: a density functional theory approach, J. Phys. Chem., 97 (1993) 4786-4796. http://dx.doi.org/10.1021/j100120a035
[34] N.A. Seaton, J.P.R.B. Walton, N. quirke, A new analysis method for the determination of the pore size distribution of porous carbons from nitrogen adsorption measurements, Carbon, 27 (1989) 853-861. http://dx.doi.org/10.1016/0008-6223(89)90035-3
[35] Z. Zhang, Z. Yang, Theoretical and practical discussion of measurement accuracy for physisorption with micro- and mesoporous materials, Chinese J. Catal., 34 (2013) 1797-1810. http://dx.doi.org/10.1016/s1872-2067(12)60601-9
[36] P.I. Ravikovitch, A.V. Neimark, Characterization of Micro- and Mesoporosity in SBA-15 Materials from Adsorption Data by the NLDFT Method, J. Phys. Chem. B, 105 (2001) 6817-6823. http://dx.doi.org/10.1021/jp010621u
[37] G. Engelhardt, D. Michel, High-resolution solid-state NMR of silicates and zeolites, John Wiley and Sons,New York, NY, United States, 1987.
[38] G. Kowalczyk, J.E. Roberts, Solid State 29Si NMR determination of crystalline silica in natural iron oxide pigments, Anal. Chim. Acta, 286 (1994) 25-35. http://dx.doi.org/10.1016/0003-2670(94)80173-8
[39] R.A.B. Devine, Macroscopic and microscopic effects of radiation in amorphous SiO2, Nucl. Instrum. Methods Phys. Res. B, 91 (1994) 378-390. http://dx.doi.org/10.1016/0168-583x(94)96253-7
[40] T.A. Dellin, D.A. Tichenor, E.H. Barsis, Volume, index- of- refraction, and stress changes in electron- irradiated vitreous silica, J. Appl. Phys., 48 (1977) 1131-1138. http://dx.doi.org/10.1063/1.323791

[41] J. Li, C. Fan, Q. Li, H. Wang, X. Zhang, In situ studies on irradiation resistance of nanoporous Au through temperature-jump tests, Acta Mater., 143 (2018) 30-42. http://dx.doi.org/10.1016/j.actamat.2017.09.054
[42] A.M. Manzini, M.A. Alurralde, G. Giménez, V. Luca, The radiation response of mesoporous nanocrystalline zirconia thin films, J. Nucl. Mater., 482 (2016) 175-186. http://dx.doi.org/10.1016/j.jnucmat.2016.10.019
[43] A. Manzini, M. Alurralde, V. Luca, Radiation response of cubic mesoporous silicate and borosilicate thin films, Nucl. Instrum. Methods Phys. Res. B, 415 (2018) 54-63. http://dx.doi.org/10.1016/j.nimb.2017.10.026
[44] Y. Lou, B. Siboulet, S. Dourdain, M.R. Rafiuddin, X. Deschanels, J.-M. Delaye, Molecular dynamics simulation of ballistic effects in mesoporous silica, J. Non-Cryst. Solids, 549 (2020) 120346. http://dx.doi.org/10.1016/j.jnoncrysol.2020.120346
[45] S. Klaumünzer, Radiation compaction of porous Vycor glass, Nucl. Instrum. Methods Phys. Res. B, 166-167 (2000) 459-464. http://dx.doi.org/10.1016/s0168-583x(99)00696-5
[46] S. Klaumünzer, Radiation compaction of nanoporous Vycor glass, Nucl. Instrum. Methods Phys. Res. B, 191 (2002) 356-361. http://dx.doi.org/10.1016/s0168-583x(02)00536-0
[47] Y. Lou, G. Toquer, S. Dourdain, C. Rey, C. Grygiel, D. Simeone, X. Deschanels, Structure evolution of mesoporous silica SBA-15 and MCM-41 under swift heavy ion irradiation, Nucl. Instrum. Methods Phys. Res. B, 365 (2015) 336-341. http://dx.doi.org/10.1016/j.nimb.2015.08.009
[48] J.A.C. Marples, Dose rate effects in radiation damage to vitrified radioactive waste, Nucl. Instrum. Methods Phys. Res. B, 32 (1988) 480-486. http://dx.doi.org/10.1016/0168-583x(88)90258-3
[49] R.A.B. Devine, J.P. Duraud, E. Dooryhée, Structure and imperfections in amorphous and crystalline silicon dioxide, Wiley2000.
[50] M. Toulemonde, S.M.M. Ramos, H. Bernas, C. Clerc, B. Canut, J. Chaumont, C. Trautmann, MeV gold irradiation induced damage in α-quartz: Competition between nuclear and electronic stopping, Nucl. Instrum. Methods Phys. Res. B, 178 (2001) 331-336. http://dx.doi.org/10.1016/s0168-583x(00)00496-1
[51] H. Inui, H. Mori, T. Sakata, H. Fujita, Electron irradiation induced crystalline-to-amorphous transition in quartz single crystals, J. Non-Cryst. Solids, 116 (1990) 1-15. http://dx.doi.org/10.1016/0022-3093(90)91039-t